RESEARCH ARTICLE

DOI:10.61558/2993-074X.3469 **Article ID:** 1006-3471(2024)00-0000-00

Http://electrochem.xmu.edu.cn

Optimization of channel structure of alkaline water electrolyzer by using expanded mesh as bipolar plate

Hai-Yan Xiong [a], Zhen-Xiao Zhu [a], Xin Gao [a], Chen-Ming Fan [a], Hui-Bao Luan [b, *] and Bing Li [a, *]

a School of Mechanical and Power Engineering
East China University of Science and Technology
Shanghai 200237, China
E-mail: bingli@ecust.edu.cn
b Shanghai Marine Diesel Engine Research Institute
Shanghai 201108, China
E-mail: luanhuibao@163.com

Keywords: Alkaline water electrolyzer • expanded mesh channel structure • Numerical simulation

Abstract: Alkaline water electrolysis (AWE) is the most mature technology for hydrogen production by water electrolysis. Alkaline water electrolyzer consists of multiple electrolysis cells, and a single cell consists of a diaphragm, electrodes, bipolar plates and end plates, etc. The existing industrial bipolar plate channel is concave-convex structure, which is manufactured by complicated and high-cost mold punching. This structure still results in uneven electrolyte flow and low current density in the electrolytic cell, further increasing in energy consumption and cost of AWE. Thereby, in this article, the electrochemical and flow model of is firstly constructed, based on the existing industrial concave and convex flow channel structure of bipolar plate, to study the current density, electrolyte flow and bubble distribution in the electrolysis cell. The reliability of the model was verified by comparison with experimental data in literature. Among, the electrochemical current density affects the bubble yield, on the other hand, the generated bubbles cover the electrode surface, affecting the active specific surface area and ohmic resistance, which in turn affects the electrochemical reaction. The result indicates that the flow velocity near the bottom of the concave ball approaches zero, while the flow velocity on the convex ball surface is significantly higher. Additionally, vortices are observed within the flow channel structure, leading to an uneven distribution of electrolyte. Next, modelling is used to optimize the bipolar plate structure of AWE by simulating the electrochemistry and fluid flow performances of four kinds of structures, namely concave and convex, rhombus, wedge and expanded mesh, in the bipolar plate of alkaline water electrolyzer. The results show that the expanded mesh channel structure has the largest current density of 3330 A/m^2 and electrolyte flow velocity of 0.507 m/s in the electrolytic cell. Under the same current density, the electrolytic cell with expanded mesh runner structure has the smallest potential and energy consumption. This work provides a useful guide for the comprehensive understanding and optimization of channel structures, and provides a theoretical basis for the design of large-scale electrolyzer.

Introduction

Traditional fossil fuels not only have limited reserves, but also caused high carbon emissions and serious greenhouse effect. In recent years, renewable clean energy, including solar energy, wind energy, etc., has been booming in the world to replace traditional fossil fuels and achieve energy transformation[1-5]. Hydrogen energy, a clean secondary energy of high thermal value, as energy carriers and raw materials, widely used in renewable energy integration, metallurgy, synthetic ammonia, and hydrogen-synthetic fuel, etc.[6-10] Among various hydrogen production methods, electrolytic water hydrogen is the cleanest hydrogen production technology, and currently accounts for only about 5%, but it is predicted that it has high potential market value[11-16].

Electrolytic water hydrogen production[17-22] is divided into: alkaline water electrolysis (AWE)[23-26], proton exchange membrane electrolysis (PEM)[27, 28], solid oxide electrolysis (SOEC) and anion exchange membrane electrolysis (AEM). Among them, AWE is currently the most mature and lowest cost electrolytic hydrogen production technology with a single cell scale of 3000Nm^3/h, has achieved a large-scale industrialized hydrogen production[19]. However, the cost for the AWE is still far higher than the conventional hydrogen production technology, such as reforming fossil fuels (coals, natural gas, etc.). Therefore, it is urgent to further lower the cost and increase market competition of AWE.

Cost reduction can be achieved by reducing the cost of electrolyzer equipment and improving the efficiency of the electrolyzer. Alkaline water electrolyzer is mainly composed of electrodes, diaphragm, bipolar plates and end plates, etc. Traditionally, the bipolar plate of AWE has concave-convex structure that is complicated and difficult to be fabricated by mold punching with high manufacturing costs. Besides, AWE has lower current density and high energy consumption problems. Currently industrial concave-convex bipolar plates exist the problem of uneven electrolyte flow. The uneven flow of

electrolyte hinders the ion and heat transfer on the electrode surface, and the bubbles without escape in time accumulate on the electrode, reducing the active specific surface area of the electrode and increasing the activation overpotentials and ohmic drop, then increasing the energy consumption and cost of AWE[19, 29, 30]. Therefore, it is necessary to improve the uniformity of the electrolyte distribution and bubble escape by optimizing the bipolar plate channel structure[30-35].

Modeling is an essential tool for the rapid development of AWE, which is benefit to channel structure 、 process parameters optimization and analysis of large-scale electrolyzer[18, 36-38]. Regarding the modeling of AWE, modeling research firstly focused on the 2D physical field analysis, such as thermodynamics, flow, heat transfer, without involving in flow field structure and experimental verification. For example, Hammoudi et al.[37] proposed a 2D multi-physical model describing the evolution of the operating voltage of an electrolysis based on electrochemistry, thermodynamics and two-phase flow. Olivier et al.[36] reviewed the 2D electrochemical and heat transfer (lumped heat capacity method) models of AWE electrolysis, without considering the flow field structure and mass transfer model of AWE. Hu et al.[39] made a detailed and comprehensive review of the existing modeling work on 2D AWE thermodynamics, electrochemistry, heat and gas purity.

Recently, Huang et al.[38] established a 3D traditionally integrated channel structure model, considering the bubble effect, the coupling equation of electrochemical and mixture model for the two-phase laminar flow. The results show that when the current density is higher than 2500 A/m^2, the relative error of the model's current-voltage (I-V) characteristic curve is less than 5%. Further, Zhang et al.[40] modeled and simulated the spherical concave and convex (SCC) Euler-Euler RANS *k-ε* turbulence model, proving the SCC-shaped bipolar plate structure could effectively average the electrolyte and bubbles distribution in the channel and reduced the hydrogen gas concentration on the electrode surface by comparing with the straight channel, which was conducive to the improvement of electrolytic efficiency. Besides, Wang[41] et al. also established a 3D laminar model to study the uniformity of liquid flow in the concave-convex bipolar plate (CCBP) electrolyzer, and combined with visual experiments to verify the simulation results, revealed the obvious non-uniform flow in the CCBP electrolyzer. Subsequently, Wang et al[42] compared the flow uniformity of blank, CCBP, wedge, and rhombus electrolyzer by using a laminar flow model, and compared with that of conventional CCBP electrolyzer, the flow uniformity of wedge and CCBP electrolyzer was respectively increased by 19% and 28%. Zhao et al[43, 44] design an industrial system-level AWE hydrogen production equipment, comparing the concave-convex structure and expanded mesh structure as bipolar plate by experiments. There are some literatures concerning simulation models of 3D alkaline water electrolyzer channel structures, but there are very few studies of expanded mesh channel structures, and especially, until now the research about comprehensive analysis of the electrochemical and flow performances within the electrolytic cells of expanded mesh channel structures have not yet been comprehensively reported from the perspective of theoretical studies.

In this paper, we firstly establish an electrochemical and RNG κ-ε phase transfer mixture model based on the industrial concave-convex bipolar plate channel structure. The model is verified with the experimental values in the literature, which ensures the accuracy and reduces the calculation cost. Secondly, the simulation and comparison of bipolar plate electrolytic cell with concave-convex, rhombus, wedge and expanded mesh structures were carried out to study the optimal bipolar plate channel structure, analyze its internal electrochemistry and flow field distribution, and achieve the goal of reducing energy consumption and cost of AWE.

Methodology

Geometric modelling

The large alkaline water electrolyzer consists of multiple electrolytic cells, in which the structure is identical of each electrolytic cell, so this paper firstly focuses on a single electrolytic cell. Zero-gap electrolytic cell structure is adopted to reduce the internal resistance of electrolyte and improve the electrolysis efficiency by reducing the distance between electrodes and diaphragm. As shown in **Figure 1**, The geometrical model of a zero-gap alkaline water electrolytic cell consists of a cathode, anode, diaphragm, and cathodic and anodic flow channel field (the flow channel between the bipolar plate and the electrode), and we focus on the effect of the bipolar plate structure. Wherein, the 3D porous electrode and diaphragm domains are assumed to be homogeneous cylindrical domains of porosity 0.27 and 0.56, respectively[45].

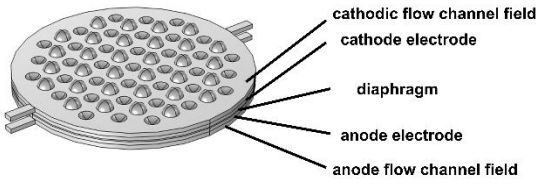

Figure 1. filter-press type alkaline water electrolysis cell

Figure 2 (a-d) shows the geometrical models of the concave-convex, rhombus, wedge and expanded mesh flow field structures on the bipolar plate. The single unit of the rhombus structure is a square with a height of 2 mm; the single unit of the rhombus structure is a rhombus formed by the stacking of two rectangles, with the length of the rectangles 2.5 mm, half the width of the length and the height of the rhombuses 2.5 mm; and the expanded mesh structure consists of a staggered structure with a long intercept of 12 mm, a short intercept of about 8.5 mm, and a total thickness of 2.33 mm, the model parameters are shown in **Table 1**.

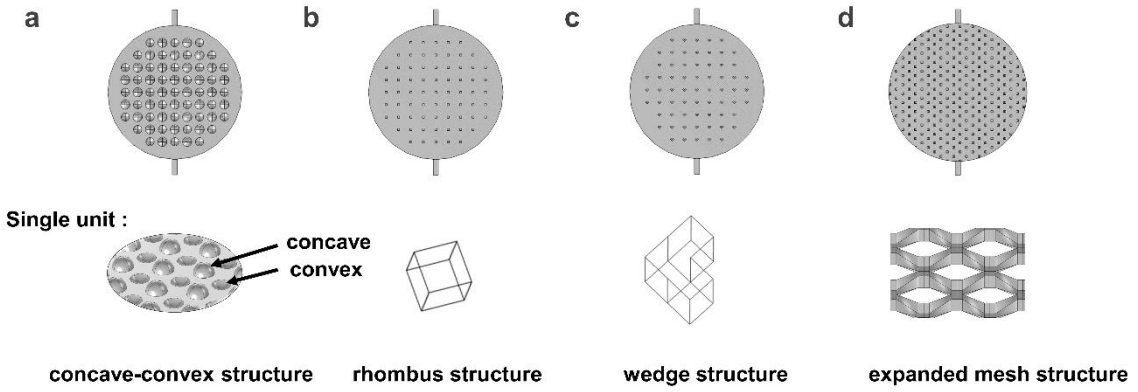

Figure 2. (a) concave-convex structure flow path (b) rhombus structure flow path (c) wedge structure flow path (d) expanded mesh structure flow path

Table 1 Four types of bipolar plate flow field structure dimensions

	geometric parameters	value(mm)
	electrode radius	65
	electrode height	2
	diaphragm radius	65
	diaphragm height	0.7
	inlet length	6
	inlet width	6
	channel radius	65
	channel height	2
Single unit		
concave-convex	Concave/ convex sphere radius	4.5
	concave and convex spheres	12
rhombus	height	2
	channel height	3
wedge	length	2.5
	width	1.25
	height	2.5
	channel height	3
expanded mesh	thickness	0.5
	height	2.33
	transverse distance	6
	longitudinal distance	4.23

Mathematical models of the electrolyzer cell

Electrochemical model

Alkaline water electrolysis overall reactions:

Cathode reaction: $2H_2O\text{-}2e^- \rightarrow 2OH^- + H_2$ (1)

Anode reaction: $4OH^- \text{-} 4e^- \rightarrow 2H_2O + O_2$ (2)

There are mainly three kinds of overpotential in a single cell:

(1) Activation overpotential;

(2) Ohmic overpotential;

(3) Diffusion overpotential;

Alkaline water electrolytic cell has ignored concentration overpotential due to low current densities and high OH^- concentrations[46, 47]. Thereby, only the activation overpotential and ohmic overpotential are considered, and the equations are as follows:

$$E_{cell}=E_{rev}+E_{act,ano}+E_{act,cat}+E_{ohm} \quad (3)$$

Where E_{rev} is the reversible voltage of a single cell, $E_{act,ano}$ and $E_{act,cat}$ are the activation overpotentials of the anode and cathode, respectively, E_{ohm} is an ohmic overpotential.

According the Nernst equation[48]:

$$E_{rev}=E^0_{rev}+\frac{R*T}{2*F}\ln\frac{P_{H2}\sqrt{P_{O2}}}{P_{H2O}} \quad (4)$$

P_{H2} , P_{02} and P_{H2O} are the partial pressures of H_2、 O_2 and H_2O. Assuming that the concentration of each substance is the same everywhere, $C_{PE}=C_{PS}$, $C_{RE}=C_{RS}$, the activation overpotential-current relationship follows the Butler-Volmer equation[48]:

$$i_{loc} = i_0\left[e^{\left(\frac{\alpha_a*F*\eta}{R*T}\right)} - e^{\left(\frac{-\alpha_c*F*\eta}{R*T}\right)}\right] \quad (5)$$

where i_{loc} means the current density at the electrode, i_0 is the exchange current density, α_a , α_c are the electrode electron transfer factors, F is Faraday's constant, F=96485.33C/mol, R is the molar gas constant, and T means the temperature.

For both cathodic and anodic electrode reactions, when cathodic and anodic polarization dominate respectively, the overpotentials conform to the Tafel equation as shown in (6~7)[48]:

$$E_{act,a} = \frac{RT}{n*\alpha_a*F} * ln\frac{i_{loc}}{i_{0,a}} \quad (6)$$

$$E_{act,c} = \frac{RT}{n*\alpha_c*F} * \ln\frac{i_{loc}}{i_{0,c}} \quad (7)$$

The active specific surface area was determined by considering a reduction in the active area for electrochemical reactions due to bubble coverage:

$$a_v = S * (1-\theta) \quad (8)$$

a_v is the electrode reaction area, S is the specific surface area of the electrocatalyst, calculated by surface area/volume in m^2/m^3, i.e. 1/m. θ is the bubble volume fraction, calculated by flow modelling.

$$i_v = a_v * i_{loc} \quad (9)$$

The ohmic overpotential is the loss caused by the resistance of the electrodes, electrolyte and diaphragm. The total ohmic overpotential consists of the electrolyte, electrode and diaphragm overpotentials and is expressed as follows:

$$E_{\text{ohm}} = I * \left(R_a + R_c + R_{l_{bubble}} + R_{mem}\right) \quad (10)$$

Where R_a and R_c represent the anode and cathode electrode resistance, $R_{l_{bubble}}$ represents the electrolyte resistance considering the effect of bubbles, and R_{mem} means the diaphragm resistance, and the conductivity σ_{mem}=20.44 S/m[45] was set. The resistance calculation formula is as follows:

$$R = \frac{1}{\sigma} * \left(\frac{L}{S}\right) \quad (11)$$

$$\sigma_a = \sigma_c = \sigma_{Ni} = 60000000 - 279650 * T + 532 * T^2 - 0.38057 * T^3 \quad (12)$$

$$\sigma_{KOH} = 2.041 * m_{KOH} - 0.0028 * {m_{KOH}}^2 + 0.005332 * m_{KOH} * T + 207.2 * \frac{m_{KOH}}{T} + 0.001043 * {m_{KOH}}^3 - 0.0000003 * {m_{KOH}}^2 * T^2 \quad (13)$$

$$m_{KOH} = m_{wt} * \left(183.1221 - 0.56845 * T + 984.5679 * e^{\left(\frac{m_{wt}}{115.96277*5610.5}\right)}\right) \quad (14)$$

Where m_{wt} represents the alkaline water electrolysis electrolyte mass fraction, and the industrial alkaline mass fraction is 30%.

The effective conductivity of the electrolyte was corrected according to the Bruggeman equation:

$$\sigma_{l,eff} = {\varepsilon_l}^{1.5} * \sigma_l \quad (15)$$

where ε_l is the effective volume fraction of the electrolyte, and the electrode substrate is a 60-mesh Ni mesh with a porosity of 0.2695, $\varepsilon_l = 0.2695$ [45], taking into account the effect of bubbles:

$$\sigma_{l_{bubble}} = \sigma_{l,eff} * (1-\theta) \quad (16)$$

There is a difference between the current conservation equation and the potential equation at the electrode-electrolyte interface due to the presence of overpotential, as shown in Eq. (17-18):

$$i_l = -\sigma_{l,eff} * \nabla\Phi_l \qquad \nabla i_l = i_v \quad (17)$$

$$i_s = -\sigma_s * \nabla\Phi_s \qquad \nabla i_s = -i_v \quad (18)$$

where i_s (A/m²) and i_l (A/m²) denote current density vectors, Φ (V) represents the potentials in the metal conductor and electrolyte, and the subscripts s and l represent the electrodes and electrolyte, respectively.

RNG κ-ε phase transfer mixture model

This article focusses on the uniformity of the electrolyte flow, which is the basis of the overall gas-liquid flow uniformity during the electrolysis process; therefore, the electrolyte flow in an alkaline water electrolyzer can be calculated by solving the single-phase steady-state continuity equations and the Navier-Stokes equations. Water vapor and H_2/O_2 gas crossover are not considered, and the volume change that exists is between liquid water and H_2/O_2 gas, and the sum of the volume fractions of the two phases within each computational mesh is 1. Secondly, according to previous studies, the flow in alkaline water electrolyzer is of dispersive turbulence[49, 50]. Therefore, this paper established the phase transfer mixture model, which is a relatively simplified dispersion-type flow model that requires only a set of mass and momentum equations to be calculated. In addition, the RNG κ-ε model improves the model convergence by attaching a turbulent dissipation term ε to the equations. Eventually, in this paper, the RNG κ-ε phase transfer mixture model is considered to be selected to simulate the flow characteristics inside the alkaline water electrolyzer, which can lead to the following equations:

the mass conservation equation (continuity equation):

$$\nabla * (\rho\vec{u}) = 0 \quad (19)$$

Momentum conservation equation:

$$\rho(\vec{u} * \nabla)\vec{u} = \nabla * \left[-p\vec{I} + \vec{K}\right] + \vec{F} + \rho g \quad (20)$$

The turbulent flow is modeled using the κ-ε model to solve for the turbulent kinetic energy κ and turbulent dissipation ε, which are calculated as follows:

$$\rho\frac{\partial\kappa}{\partial t} + \rho(\vec{u} * \nabla)\kappa = \nabla * \left[\left(\mu + \frac{\mu_T}{\sigma_k}\right)\nabla\kappa\right] + P_k - \rho\varepsilon \quad (21)$$

$$\rho\frac{\partial\varepsilon}{\partial t} + \rho(\vec{u} * \nabla)\varepsilon = \nabla * \left[\left(\mu + \frac{\mu_T}{\sigma_\varepsilon}\right)\nabla\varepsilon\right] + C_{\varepsilon1}\frac{\varepsilon}{k}P_k - C_{\varepsilon2}\rho\frac{\varepsilon^2}{k} \quad (22)$$

$$\frac{3C_{d,i}\rho_c}{4d_i}u_{slip,i}\overrightarrow{u_{slip,i}} = -\left(\rho - \rho_{s_i}\right)\left(\frac{\partial\overrightarrow{u_m}}{\partial t} - \overrightarrow{u_m} * \nabla\overrightarrow{u_m} + g + \frac{F}{\rho}\right) \quad (23)$$

Where ρ means the density of the mixture, ρ_{s_2} is the density of the bubble phase, u means the velocity vector of the mixture, P is the fluid pressure, μ is the mixture viscosity, μ_T is the turbulent viscosity, F is the external force, g means the acceleration of gravity, u_{slip} is the slip velocity, $C_{d,i} = 0.44$; the empirical coefficients $C_{\varepsilon1} = 1.42$ and $C_{\varepsilon2} = 1.68$.

The mass sources of H_2 and O_2 are calculated by Faraday's law as following[51]:

$$m_{H_2} = \frac{i_v * M_{H_2}}{2*F} \quad (24)$$

$$m_{O_2} = \frac{i_v * M_{O_2}}{4*F} \quad (25)$$

Where i_v (A/m³) means volume current density, M_{H_2}, M_{O_2} (g/mol) means the relative molecular mass of H_2 and O_2.

Mass transfer between liquid water and gas phase in the electrode domain:

$\nabla N_i = qs_{si}$

(26)

$m_{liquid} = \pm \frac{i_v * M_{OH}}{F}$

(27)

qs_{si} (kg/m^3·s) means the mass transfer to other term, where qs_{s1} is equal to m_{liquid}, which means electrolyte transport through the diaphragm due to electrochemical reactions, positive on the hydrogen electrode domain and negative on the oxygen electrode domain; qs_{s2} is equal to m_{H_2} on the H_2 electrode domain and m_{O_2} on the O_2 electrode domain.

The electrochemical current density affects the bubble yield, on the other hand, the generated bubbles cover the electrode surface, affecting the active specific surface area, which in turn affects the electrochemical reaction, achieving a bidirectional coupling between electrochemistry and flow, as showing in **Figure 3**.

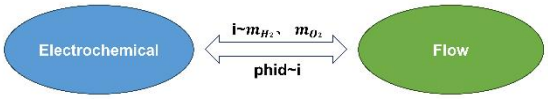

Figure 3 Electrochemical and flow multi-physics field coupling relationships

Boundary condition

The hydrogen side of the electron-conducting phase was set to be electrically grounded, and the potential of the oxygen side was constant to the electrolytic cell voltage(E).

The flow boundary conditions use velocity inlets and pressure outlets. At the inlet boundary, the electrolyte flows at 0.22 m/s and the gas phase have no flow. All external boundaries have no-slip boundary conditions.

At the inlet boundary, the gas phase volume fraction is zero. The gas-liquid phase flows out of the outlet boundary.

Mesh independency test

The entire geometric model is assembled using a combine, where adjacent domain boundaries share the same mesh and boundary conditions. Mesh types are divided into structured and unstructured mesh. As shown in **Figure 4**(a-b), the diaphragm domain, inlet and outlet are divided into structured hexahedral mesh due to regular geometry, significantly reducing the number of meshes. Channel region due to the spherical convex-concave surface structure, can only be divided by unstructured free tetrahedral meshes.

The independence of the mesh is verified, and the difference between the calculated results of O_2 current density, and average flow velocity in the Mesh1-4, is 0.02%, 0.31%, 0.32% and 2.05%, respectively, as shown in **Table 2**, and it can be concluded that the calculated results no longer change with the change of the number of meshes. Therefore, considering the calculation accuracy and calculation quantity, the Mesh3 was selected for numerical simulation calculation.

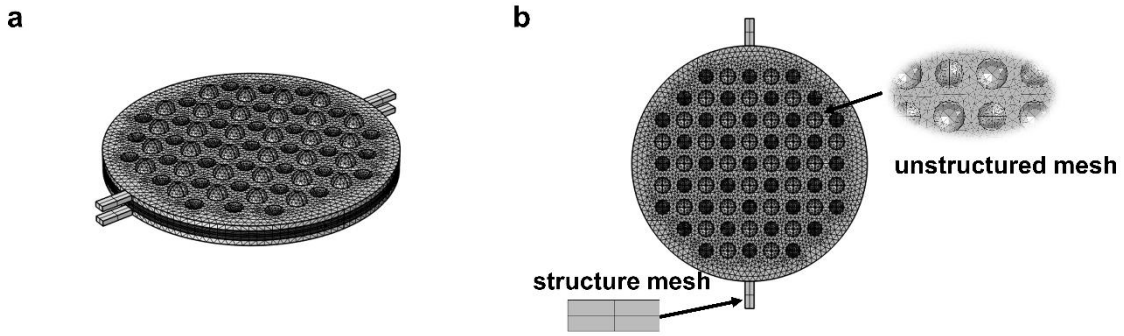

Figure 4. Mesh delineation of filter press electrolyzer with concave-convex structure (a) main view (b) top view

Table 2 Mesh-independence validation calculations

Mesh type	Mesh1	Mesh2	Mesh3	Mesh4
Number of domain cells	14100	29466	102702	926090
Average cell mass	0.47	0.65	0.68	0.65
O_2 current density	2449.5	2457.5	2459.8	2460.3
O_2 Relative rate of change	0.44%	0.11%	0.02%	Baseline
Average flow velocity	0.00882	0.00900	0.00904	0.00922
Relative change rate	4.39%	2.39%	2.05%	Baseline

Solving method

Firstly, the study step was initialized using the current density distribution to obtain good initial values which are used to improve the convergence of the model. Next, the solution is solved using a steady state solver with fully coupled calculations, using an iterative approach step by step rather than through a

single computationally intensive step with a relative tolerance of less than 10^{-4}.

Model verification

The reliability of the model was verified by comparing with the voltage-current density curves of large electrolyzer operation in the Guo et al literature[45], which is an important indicator for evaluating the performance of electrolyzer, and the model parameters are shown in **Table 3**.

Table 3 Physical field parameters[32, 45, 52]

Physical Field Parameter	Unit	Value
Electrolyte concentration	mol/L	6.72
Electrolyte conductivity	S/m	138
H2 side exchange current density	A/m^2	23.4
O2 side exchange current density	A/m^2	9.3
exchange current density (α_a, α_c)		0.5
electrolytic cell voltage	V	2
Diaphragm conductivity	S/m	20.44
Electrolyte inlet flow velocity	m/s	0.22
Electrolyzer pressure	MPa	2
Operating temperature	°C	90

Figure 5(a) shows the current status of alkaline electrolyzer energy consumption up to 2018, from which it can be seen that the electrolytic cell voltage is between 1.6V and 2.2V under real working conditions. The comparison graph of this paper with the experimental data in the literature[45] through the model results is shown in **Figure 5**(b). From the graph, it can be seen that the I-V curve calculated by the above simulation model in this paper has the same trend with the experimental result reported in the literature, and the error is within the acceptable range, thus the numerical simulation method in this paper is considered to be effective and capable of judging correctly the electrochemical performance and the electrolyte flow distribution within the electrolytic cell.

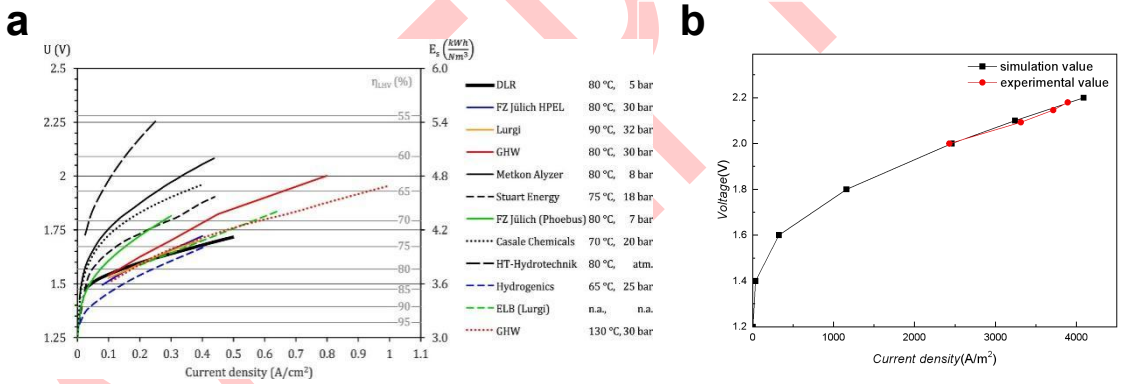

Figure 5 (a) Typical polarization curves (b) Comparison of simulated (black line) and experimental values (red line) of current density-voltage polarization curves of alkaline water electrolyzer[45, 53]

Results and discussion

Electrolytic cell performance

Electrochemical performance

Figure 6 (a-b) shows the current density distribution of the electrolyte in the electrolytic cell at Q=0.6 m^3/h and E=2.0 V. It can be seen that, the closer to the separator center (Hz=0.35 mm), the higher the current density of the electrolyte, with the maximum value of the current density up to 3050 A/m^2; And the closer to the bipolar plate flow channel interface (Hz=2.7 mm), the lower the current density of the electrolyte. In addition, a significant decrease in current density in the electrode and diaphragm domains is clearly seen, with a very small current density gradient and a small voltage drop in the channel domain.

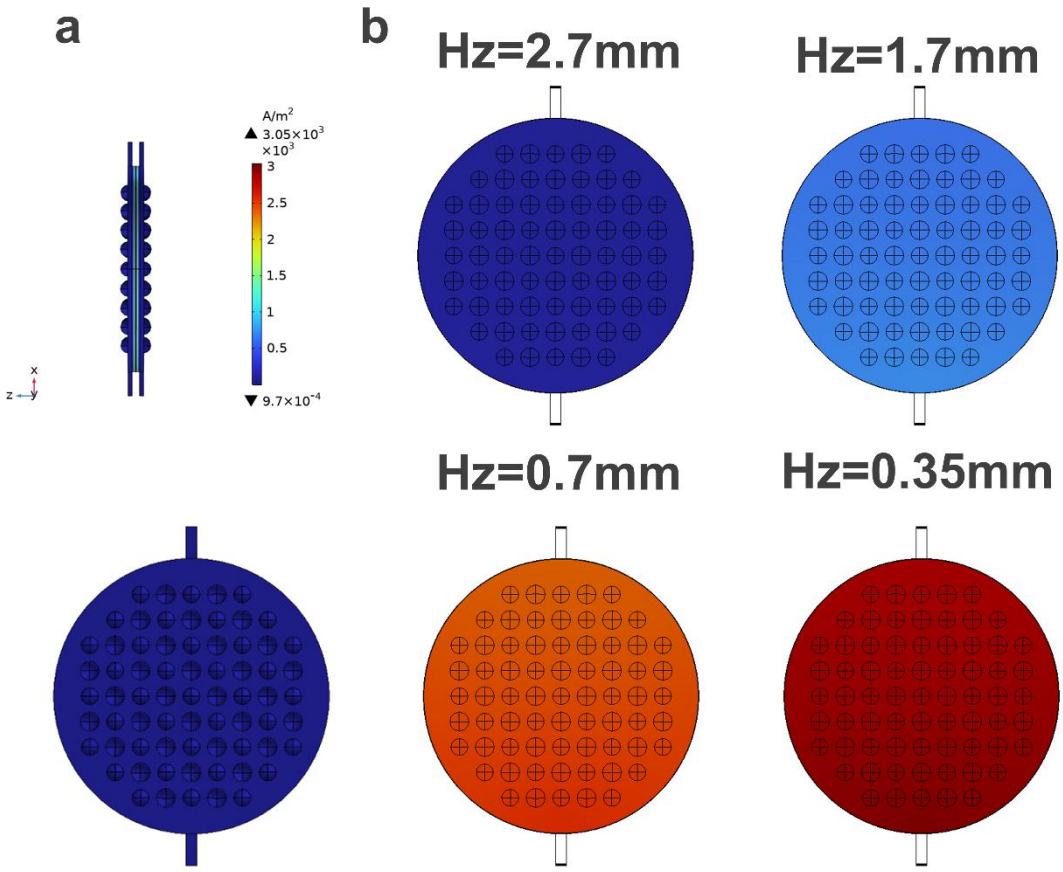

Figure 6. (a) Side view and main view of the current density distribution of the electrolyte inside the electrolytic cell (b) Main view of the current density distribution of the electrolyte at different height

Figure 7(a-b) shows the current density distribution on the electrode within the electrolytic cell, and the trend of current density distribution of the electrolyte is opposite to that of **Figure 6**, the closer to the bipolar plate (Hz=2.7 mm), the higher the current density on the electrode surface, and the closer to the diaphragm (Hz=0.7 mm), the lower the current density on the electrode, which is due to the co-existence of both electronic and ionic conduction within the electrolytic cell, and when close to the diaphragm, the ionic conduction is dominant, the closer to the bipolar plate channel interface, electronic conduction is dominant, the electrolyte current is converted into electrode current, and the current density of electrolyte decreases. Therefore, the interface where the bipolar plate is in contact with the electrode (Hz=2.7 mm) has the highest current density on the electrode.

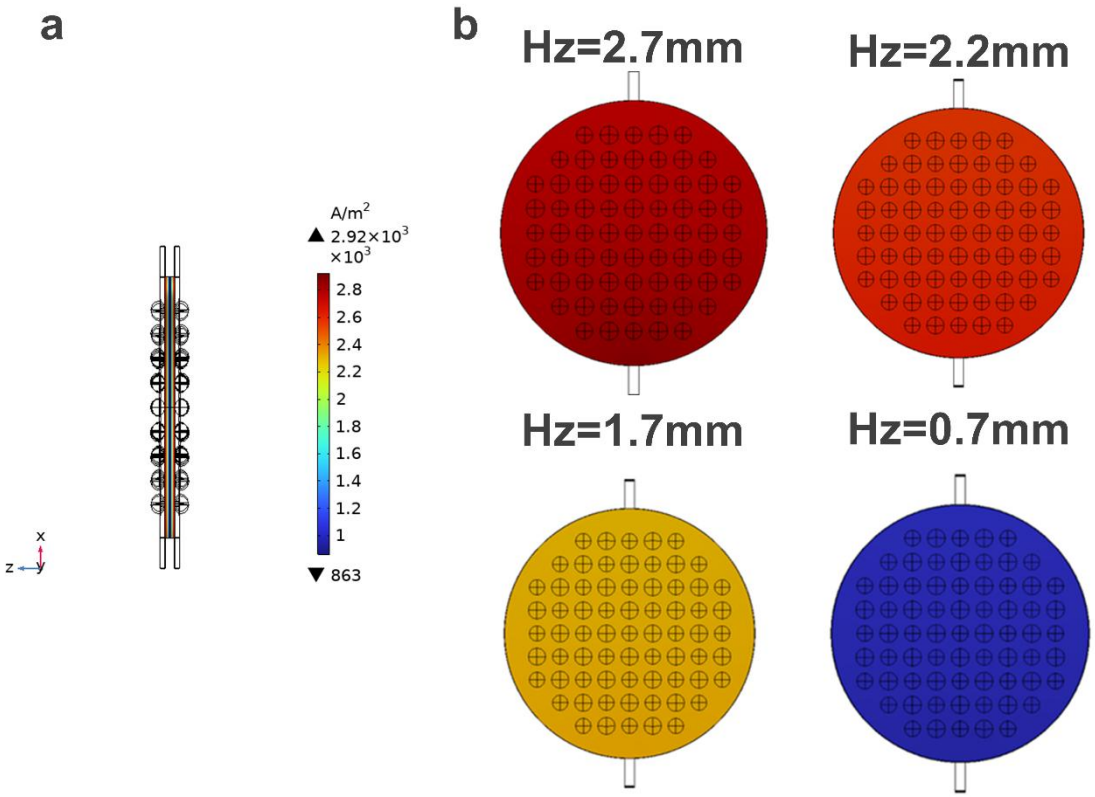

Figure 7. (a) Side view of the current density distribution on the electrodes inside the electrolytic cell (b) Main view of the current density distribution on the electrodes at different height interfaces

As can be seen from **Figure 8**, the electrode current density gradually decreases along the x direction of the outlet, considering the reason is that the bubbles are affected by buoyancy and gather towards the outlet, resulting in the closer the outlet, the electrode active specific surface area decreases and the bubble resistance increases.

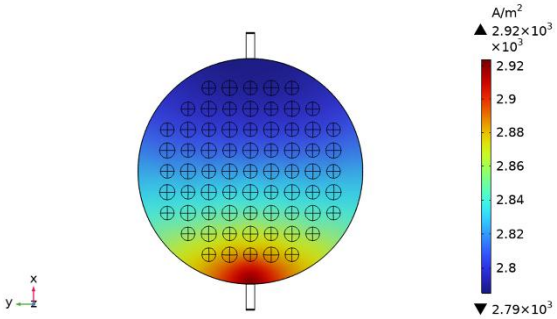

Figure 8. Main view of electrode current density at Hz= 2.7 mm (electrode-bipolar plate contact interface)

From **Figure 9**(a), it can be seen that the electrolyte current density near the inlet is maximum, and shows a decreasing trend along the outflow x direction. Combined with **Figure 9**(b), it can be seen that the concave sphere close to the inlet has the highest current density at the edge, which is considered to be due to the increase in the flow cross-sectional area of the electrolyte when it enters the concave sphere, resulting in a decrease in the flow velocity and a decrease in the current density. At the bottom of the convex sphere in contact with the electrode, the flow cross-sectional area decreases, the flow velocity increases and the current density is the maximum. Along the outlet x-direction, the current density inside the convex spheres decreases accordingly, and it is considered possible that the part of the convex spheres in contact with the electrodes is also affected by the bubbles, which leads to a decrease in the current density.

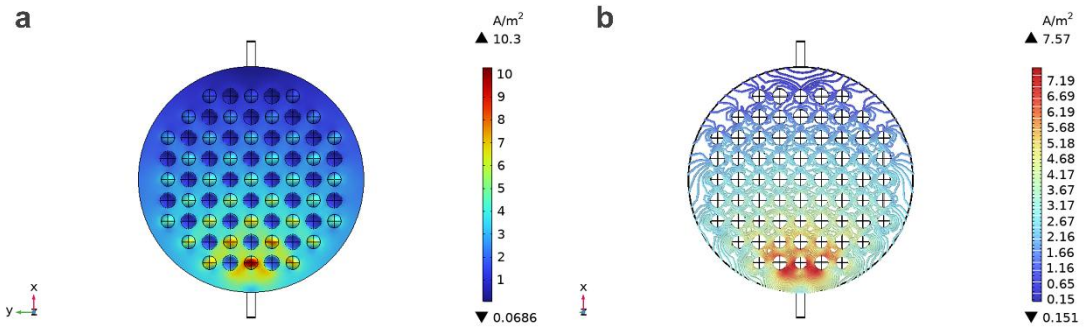

Figure 9. (a) Electrolyte current density distribution in bipolar plate concave-convex channel field (b) Electrolyte current density contour plot

Flow distribution

The electrolyte flow velocity distribution inside the electrolysis cell is shown in **Figure 10**. From **Figure 10** (a), (b), (c) and (d), it can be seen that the concave-convex structure of the flow channel leads to the uneven flow of the electrolyte, and on the same cross-section the flow velocity distribution is more uniform as closer to the center (x=0mm), which is attributed to the equal flow resistance at symmetric positions. Combined with **Figure 10** (b) and (e), it can be seen that along the outlet x direction, the flow velocity on the surface of the convex sphere tends to decrease and then increase, and the minimum flow velocity is on the cross-section of x = -24 mm. **Figure 10** (f) confirms there exists the vortices inside the concave-convex structure.

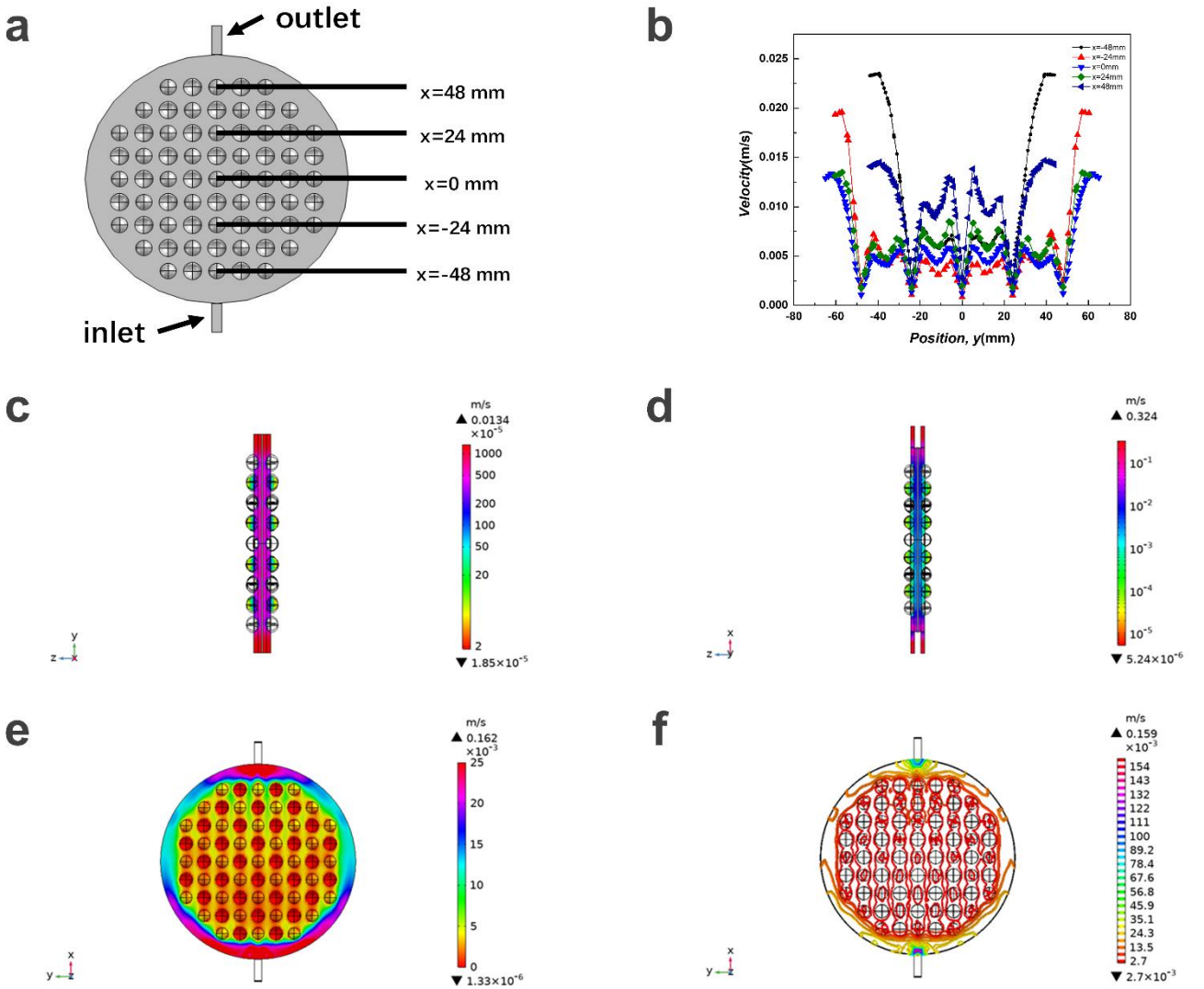

Figure 10 (a) Locations of the transversal line for study (x-y plane, z = 2.7 mm) (b) Velocity profile on the transversal line at different y positions on the reference x-y plane (z = 2.7 mm) (c) x=0 section flow velocity map (d) y=0 section flow velocity map (e) Electrolyte flow velocity distribution inside the electrolytic cell (f) Flow velocity contours

As shown in **Figure 11**(a-b), the volume fraction on the H_2 side is nearly twice as large as that on the O_2 side, with maximum volume fractions of 11.3% and 6.05%, respectively, due to the fact that the rate of generation of H_2 is twice that of O_2. As the bubbles are influenced by buoyancy and thrust, they are continuously aggregated upwards. The non-uniformity of bubble distribution originates from the non-uniform distribution of electrolyte flow, which leads to the uneven distribution of current density, increased local resistance, reduced active reaction area, increased voltage, and limited electrochemical reaction.

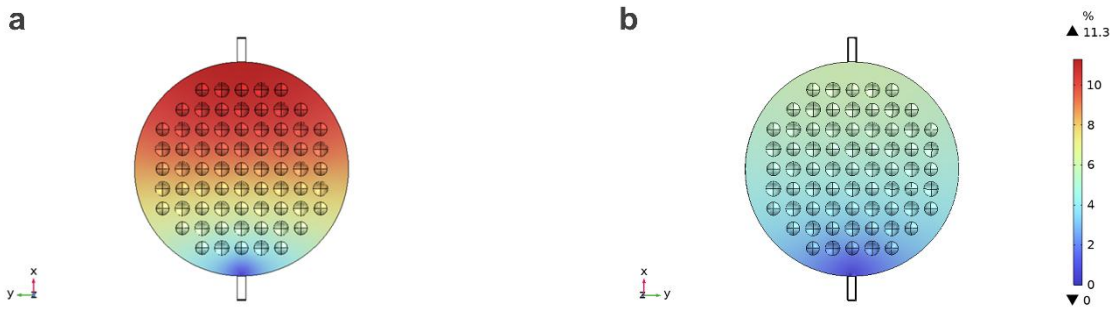

Figure 11. (a) H_2 distribution in cathode flow path (b) O_2 distribution in anode flow path

Effect of different bipolar plate flow field structures

In the electrolytic cell of the concave-convex structure bipolar plate, the electrolyte flow is unevenly distributed. Secondly, the industrial concave-convex structure bipolar plates are shaped by mold punching with high processing accuracy and cost. Therefore, it is proposed to simulate and compare the bipolar plate electrolytic cells with rhombus 、 wedge and expanded mesh structures to study the internal electric field and flow velocity distribution of the four bipolar plate channel structures, with the same computational model, boundary conditions and mesh selection as above. The current density-voltage polarization curves for the concave-convex, rhombus, wedge and expanded mesh are shown in **Figure 12**, from which it can be seen that the bipolar plate channel structure with expanded mesh has the lowest voltage, the lowest power and significantly higher electrochemical performance than the remaining three structures at the same current density.

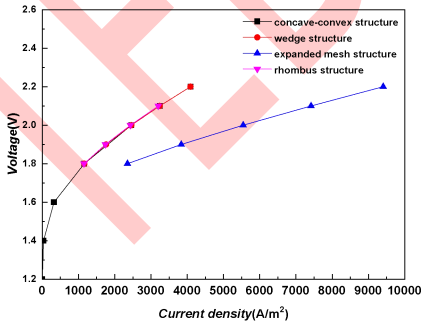

Figure 12. Four types of channel structure I-V curve

As can be seen in **Figure 13**(a-d), the expanded mesh structure has the greatest current density. The reason is that as described above, the current conduction is divided into electron conduction and ion conduction. With the increase of contact sites between the expanded mesh and the electrode, the enhancement of electron conduction leads to a significant increase in current density. Besides, the other three structures show a large current density at the inlet, decreasing along the x outlet direction, while along the x-exit direction, the current densities are significantly reduced due to the effect of bubble blocking.

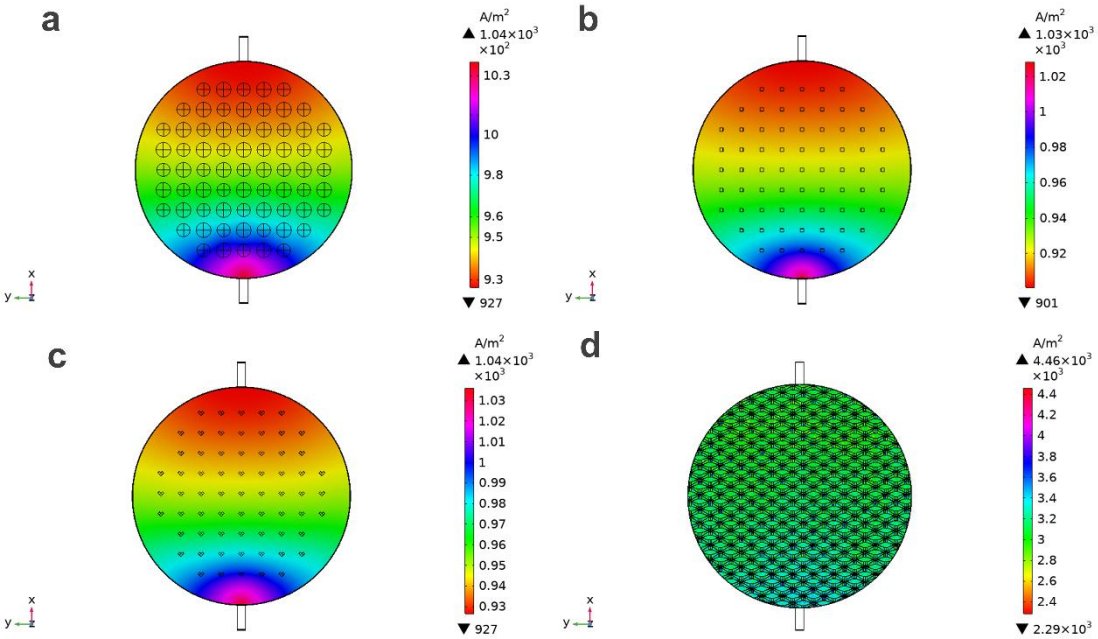

Figure 13. Current density distribution (a) concave-convex structure (b) rhombus structure (c) wedge structure (d) expanded mesh structure

From **Figure 14**(a-e), it can be seen that the flow velocity distribution of the four bipolar plate channel structures is ranked as follows: expanded mesh structure > wedge structure > rhombus structure > concave-convex structure. Expanded mesh structure is the most uniform bipolar plate channel structure among the four structures, with a maximum flow velocity of 0.507 m/s, which not only enhances the lateral flow of electrolyte and improves the flow uniformity in the x-direction, but also greatly alleviates the existence of low-speed tailing area of wedge structure through the staggered structure, which improves the uniformity of flow velocity in the y-direction, and ultimately improves the overall flow uniformity significantly.

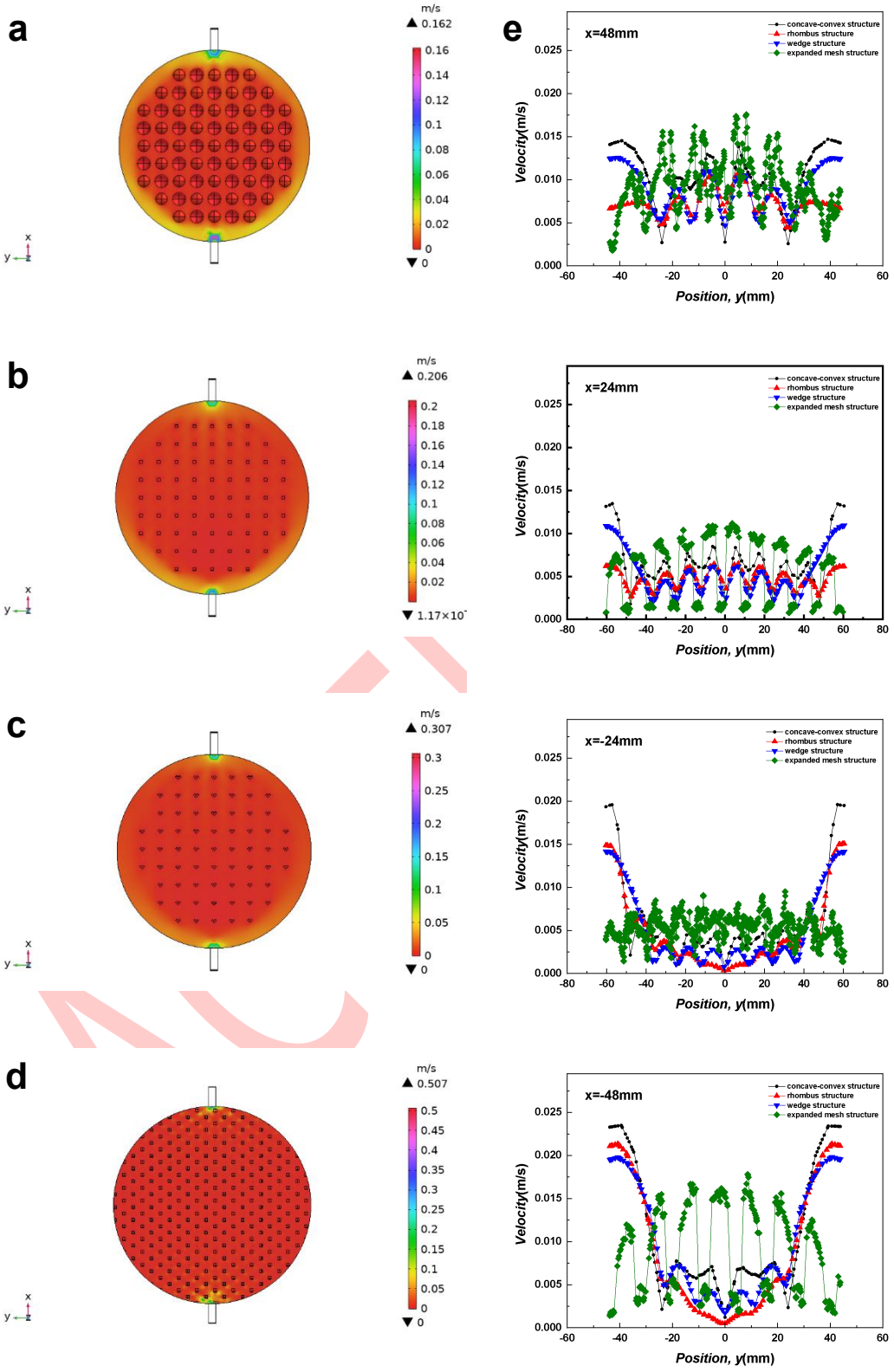

Figure 14. Electrolyte flow velocity distribution (a) concave-convex structure electrolyte flow velocity distribution (b) rhombus structure electrolyte flow velocity distribution (c) wedge structure electrolyte flow velocity distribution (d) expanded mesh structure electrolyte flow velocity distribution (e) Velocity profile on the transversal line at different y positions on the reference x-y plane (z = 2.7 mm)

Conclusion

In this paper, the electrochemical performance and electrolyte flow velocity distribution of electrolytic cell with four different bipolar plate channel structures, namely, concave-convex, rhombus、wedge and expanded mesh, were simulated, and the following conclusions can be made:

In the electrolysis cell of the concave-convex structure, the flow velocity on the surface of the convex sphere decreases and then increases along the x-direction of the outlet, with a minimum flow velocity on the x = -24 mm cross-section. The presence of vortices in the flow channel domain of the concave-convex structured electrolytic cells has also been confirmed.

The current density-voltage polarization curves of four bipolar plate structures, concave-convex, rhombus, wedge and expanded mesh, were compared, and at the same current density, the expanded mesh structure had the lowest voltage and the lowest energy consumption.

Expanded mesh structure is the most uniform bipolar plate channel structure among the above four structures, with a maximum flow velocity of 0.507 m/s,

This work provides useful guidance for the optimization design of electrolytic cell structure. In the future research, the selection of expanded mesh structure and local structure optimization are carried out to improve the performance of the electrolytic cell, supplemented by experimental observation and verification.

Acknowledgements

This work was financially supported by the National Natural Science Foundation of China (No. 52074130) and the Engineering Research Center of Resource Utilization of Carbon-containing Waste with Carbon Neutrality Ministry of Education.

References

[1] Steven Chu, Arun Majumdar. Opportunities and Challenges for a Sustainable Energy Future[J]. Nature,2012, 488(7411): 294-303.

[2] Xi Yang, Chris P. Nielsen, Shaojie Song, and Michael B. McElroy. Breaking the Hard-to-Abate Bottleneck in China's Path to Carbon Neutrality with Clean Hydrogen[J]. Nature Energy,2022, 7(10): 955-965.

[3] Jeffrey D. Sachs, Guido Schmidt-Traub, Mariana Mazzucato, Dirk Messner, Nebojsa Nakicenovic, Johan Rockström, Nakicenovic N, Rockström J. Six Transformations to Achieve the Sustainable Development Goals[J]. Nature Sustainability,2019, (No.9): 805-814.

[4] Yanbin Li, Weikun Hu, Feng Zhang, Yun Li. Collaborative Operational Model for Shared Hydrogen Energy Storage and Park Cluster: A Multiple Values Assessment[J]. Journal of Energy Storage,2024, 82: 110507.

[5] Jinchao Li, Ya Xiao, Shiqiang Lu. Optimal Configuration of Multi Microgrid Electric Hydrogen Hybrid Energy Storage Capacity Based on Distributed Robustness[J]. Journal of Energy Storage,2024, 76: 109762.

[6] Umair Yaqub Qazi. Future of Hydrogen as an Alternative Fuel for Next-Generation Industrial Applications; Challenges and Expected Opportunities[J]. Energies,2022, 15(13).

[7] Marc Prewitz, Andreas Bardenhagen, Ramon Beck. Hydrogen as the Fuel of the Future in Aircrafts – Challenges and Opportunities[J]. International Journal of Hydrogen Energy,2020, 45(46): 25378-25385.

[8] Wonjae Choi, Sanggyu Kang. Greenhouse Gas Reduction and Economic Cost of Technologies Using Green Hydrogen in the Steel Industry[J]. Journal of Environmental Management,2023, 335: 117569.

[9] H. Ibrahim, A. Ilinca, J. Perron. Energy Storage Systems—Characteristics and Comparisons[J]. Renewable and Sustainable Energy Reviews,2008, 12(5): 1221-1250.

[10] Mathew Aneke, Meihong Wang. Energy Storage Technologies and Real Life Applications – a State of the Art Review[J]. Applied Energy,2016, 179: 350-377.

[11] ZiYou Yu, Yu Duan, Xing-Yu Feng, Xingxing Yu, Min-Rui Gao, Shu-Hong Yu. Clean and Affordable Hydrogen Fuel from Alkaline Water Splitting: Past, Recent Progress, and Future Prospects[J]. Adv Mater,2021, 33(31): e2007100.

[12] F. Suleman, I. Dincer, M. Agelin Chaab. Environmental Impact Assessment and Comparison of Some Hydrogen Production Options[J]. International Journal of Hydrogen Energy,2015, (No.21): 6976-6987.

[13] Christos M. Kalamaras and Angelos M. Efstathiou. Hydrogen Production Technologies: Current State and Future Developments[J]. Conference Papers in Energy,2013, 2013: 690627.

[14] Canan Acar, Ibrahim Dincer. Comparative Assessment of Hydrogen Production Methods from Renewable and Non-Renewable Sources[J]. International Journal of Hydrogen Energy,2014, 39(1): 1-12.

[15] Wentao Huang, Bohan Zhang, Leijiao Ge, Jun He, Wenlong Liao, Peilei Ma. Day-Ahead Optimal Scheduling Strategy for Electrolytic Water to Hydrogen Production in Zero-Carbon Parks Type Microgrid for Optimal Utilization of Electrolyzer[J]. Journal of Energy Storage,2023, 68: 107653.

[16] Zhenming Liu, Yajun Deng, Peng Wang, Bohong Wang, Dongliang Sun, Bo Yu. Study on the Gas-Liquid Two-Phase Flow Patterns for Hydrogen Production from Electrolytic Water[J]. International Journal of Hydrogen Energy,2024, 60: 711-728.

[17] S. Shiva Kumar, Hankwon Lim. An Overview of Water Electrolysis Technologies for Green Hydrogen Production[J]. Energy Reports,2022, 8: 13793-13813.

[18] Frank Gambou, Damien Guilbert, ORCID,Michel Zasadzinski and Hugues Rafaralahy. A Comprehensive Survey of Alkaline Electrolyzer Modeling: Electrical Domain and Specific Electrolyte Conductivity[J]. Energies. 2022, (No.3452): 3452.

[19] Li Yangyan, Deng Xintao, Gu Junjiel, Zhang Tao, Guo Bin, Yang Fuyuan, Ouyang Minggao. Comprehensive Review and Prospect of the Modeling of Alkaline Water Electrolysis System for Hydrogen Production [J]. Automotive Engineering.2022, (Vol 44) No.4.

[20] M. Chandesris, V. Médeau, N. Guillet, S. Chelghoum, D. Thoby, F. Fouda-Onana. Membrane Degradation in Pem Water Electrolyzer: Numerical Modeling and Experimental Evidence of the Influence of Temperature and Current Density[J]. International Journal of Hydrogen Energy,2015, 40(3): 1353-1366.

[21] Stefania Siracusano, Stefano Trocino, Nicola Briguglio, Fabiola Pantò, Antonino S. Aricò. Analysis of Performance Degradation During Steady-State and Load-Thermal Cycles of Proton Exchange Membrane Water Electrolytic cells (Article)[J]. Journal of Power Sources,2020: 228390.

[22] Naiying Du, Claudie Roy, Retha Peach, Matthew Turnbull, Simon Thiele, and Christina Bock, Christina Bock. Anion-Exchange Membrane Water Electrolyzes [J]. Chemical reviews,2022, (No.13): 11830-11895.

[23] Abdelrahman S. Emam, Mohammad O. Hamdan, Bassam A. Abu-Nabah, Emad Elnajjar. Enhancing Alkaline Water Electrolysis through Innovative Approaches and Parametric Study[J]. International Journal of Hydrogen Energy,2024, 55: 1161-1173.

[24] Camilia Daoudi, Tijani Bounahmidi. Overview of Alkaline Water Electrolysis Modeling[J]. International Journal of Hydrogen Energy,2024, 49: 646-667.

[25] Bin Hu, Min Liu, Qinghai Chen, Xiaowei Zhou, Hongjing Li, Meizi He, Zhongyan Li, Rong Zhang, Yingda Huang, Tauqir A. Sherazi, Nanwen Li. Porous Polybenzimidazole Membranes Doped with Koh for Alkaline Water Electrolysis[J]. Journal of Membrane Science,2024, 694: 122388.

[26] Tao Zhang, Lingjun Song, Fuyuan Yang, Minggao Ouyang. Research on oxygen purity based on industrial scale alkaline water electrolysis system with 50Nm3 H2/h[J]. Applied Energy,2024, 360: 122852.

[27] Yuanxing Liu, Md. Tanjin Amin, Faisal Khan, Efstratios N. Pistikopoulos. Safety Analysis of Proton Exchange Membrane Water Electrolysis System[J]. Journal of Environmental Chemical Engineering,2023, 11(5): 110772.

[28] Qing Wei, Lixin Fan, Zhengkai Tu. Hydrogen production in a proton exchange membrane electrolysis cell (PEMEC) with titanium meshes as flow distributors [J]. International Journal of Hydrogen Energy,2023, 48(93): 36271-36285.

[29] Matheus T. de Groot, Joost Kraakman, Rodrigo Lira Garcia Barros. Optimal Operating Parameters for Advanced Alkaline Water Electrolysis[J]. International Journal of Hydrogen Energy,2022, 47(82): 34773-34783.

[30] Robert Phillips, Adam Edwards, Bertrand Rome, Daniel R. Jones, Charles W. Dunnill. Minimising the Ohmic Resistance of an Alkaline Electrolytic cell through Effective Cell Design[J]. International Journal of Hydrogen Energy,2017, (No.38): 23986-23994.

[31] Yanfeng Zhang. Study of influencing factors of cell voltage in filter-press type electrolyzer. [D]. Hunan University, 2015.

[32] Jun Li. Simulation Study on Flow Characteristics in the Unit of Filter-Press Water Electrolyzer. [D]. China University of Petroleum, 2020.

[33] Peng Yu, Feng Mei Wang, Tofik Ahmed Shif, Xueying Zhan, Xiaoding Lou, Fan Xia, Jun He. Earth Abundant Materials Beyond Transition Metal Dichalcogenides: A Focus on electrocatalyzing Hydrogen Evolution Reaction[J]. Nano Energy,2019, 58: 244-276.

[34] J.W. Haverkort, H. Rajaei. Voltage Losses in Zero-Gap Alkaline Water Electrolysis[J]. Journal of Power Sources,2021, 497: 229864.

[35] Liping Liu, Jinyi Wang, Zhibo Ren, Fan Wang, Tao Wang, Haijiao Guo. Ultrathin Reinforced Composite Separator for Alkaline Water Electrolysis: Comprehensive Performance Evaluation[J]. International Journal of Hydrogen Energy,2023.

[36] Pierre Olivier, Cyril Bourasseau, Pr. Belkacem Bouamama. Low-Temperature Electrolysis System Modelling: A Review[J]. Renewable and Sustainable Energy Reviews,2017, 78: 280-300.

[37] M. Hammoudi, C. Henao, K. Agbossou, Y. Dubé, M.L. Doumbia. New Multi-Physics Approach for Modelling and Design of Alkaline Electrolyzers[J]. International Journal of Hydrogen Energy. 2012, (No.19): 13895-13913.

[38] Danji Huang, Binyu Xiong, Jiakun Fang, Kewei Hu, Zhiyao Zhong, Yuheng Ying, Xiaomeng Ai, Zhe Chen. A Multiphysics Model of the Compactly-Assembled Industrial Alkaline Water Electrolytic cell[J]. Applied Energy,2022, 314.

[39] Song Hu, Bin Guo, Shunliang Ding, Fuyuan Yang, Jian Dang, Biao Liu, Junjie Gu, Jugang Ma, Minggao Ouyang. A Comprehensive Review of Alkaline Water Electrolysis Mathematical Modeling[J]. APPLIED ENERGY,2022: 120099.

[40] Zaizun Zhang, Liming Jin, Ling'ao Deng, Wenbo Li, Min Liu, Zhen Geng, Cunman Zhang. Three-Dimensional Simulation of Two-Phase Flow Distribution in Spherical Concave-Convex Shaped Flow Field for Alkaline Water Electrolyzer[J]. International Journal of Hydrogen Energy,2023.

[41] Tao Wang, Jinyi Wang, Pengjie Wang, Fan Wang, Liping Liu, Haijiao Guo. Non-uniform liquid flow distribution in an alkaline water electrolyzer with concave-convex bipolar plate (CCBP): A numerical study[J]. International Journal of Hydrogen Energy,2023, 48(33): 12200-12214.

[42] Tao Wang, Jinyi Wang, Pengjie Wang, Zhibo Ren, Xupeng Yan, Wei Wang, Weiqi Guo. Plate structure design guideline for commercial alkaline water electrolyzers (AWEs) with improved liquid flow uniformity: Multi-scale quantitative criteria and experimental validation [J]. International Journal of Hydrogen Energy,2023.

[43] Pengcheng Zhao, Jingang Wang, Wei He, Liming Sun, Yun Li. Alkaline Zero Gap Bipolar Water Electrolyzer for Hydrogen Production with Independent Fluid Path[J]. Energy Reports,2023, 9: 352-360.

[44] Pengcheng Zhao, Jingang Wang, Liming Sun, Yun Li, Haiting Xia, Wei He. Optimal Electrode Configuration and System Design of Compactly-Assembled Industrial Alkaline Water Electrolyzer[J]. Energy Conversion and Management,2024, 299: 117875.

[45] Khalid Zouhri, Seong-young Lee. Evaluation and Optimization of the Alkaline Water Electrolysis Ohmic Polarization: Exergy Study[J]. International Journal of Hydrogen Energy,2016, 41(18): 7253-7263.

[46] Shunliang Ding, Bin Guo, Song Hu, Junjie Gu, Fuyuan Yang, Yangyang Li, Jian Dang, Biao Liu, Jugang Ma. Analysis of the Effect of Characteristic Parameters and Operating Conditions on Exergy Efficiency of Alkaline Water Electrolyzer[J]. Journal of Power Sources,2022, 537: 231532.

[47] Cha Quanxue. Introduction to the dynamics of electrode processes. [M]. Science Press, 2002.

[48] YUJING GUO. STRUCTURAL DESIGN AND PERFORMANCE OPTIMIZATION OFAN ALKALINE WATER HYDROGEN ELECTROLYZER. [D], Beijing University of Chemical Technology, 2020.

[49] Damien Le Bideau, Philippe Mandin, Mohamed Benbouzid, Myeongsub Kim,Mathieu Sellier, Fabrizio Ganci and Rosalinda Inguanta. Eulerian Two-Fluid Model of Alkaline Water Electrolysis for Hydrogen Production[J]. Energies. 2020, (No.13): 3394.

[50] Xuepu Cao, Ning Zhao, Shirong Zhang, Lilong Zhou, Yongqi Hu, Jimmy Yun. Investigation of the Hydrogen Bubble Effect on the Overpotential in an Alkaline Water Electrolyzer[J]. International Journal of Hydrogen Energy,2024, 49: 47-57.

[51] Li Di. Principles of Electrochemistry. [M]. Beijing: Beijing University of Aeronautics and Astronautics Press, 2008.

[52] Lingyu Gao, Lin Yang, Chenhui Wang, Guixuan Shan, Xinyi Huo, Mengfei Zhang, Wei Li, Jinli Zhang. Three-dimensional two-phase CFD simulation of alkaline electrolyzers [J]. 电化学,2023, 29(09): 25-40.

[53] Alexander Buttler, Hartmut Spliethoff. Current Status of Water Electrolysis for Energy Storage, Mesh Balancing and Sector Coupling

1 Via Power-to-Gas and Power-to-Liquids: A Review[J]. Renewable and ...
2 Sustainable Energy Reviews,2018, 82: 2440-2454.

Entry for the Table of Contents

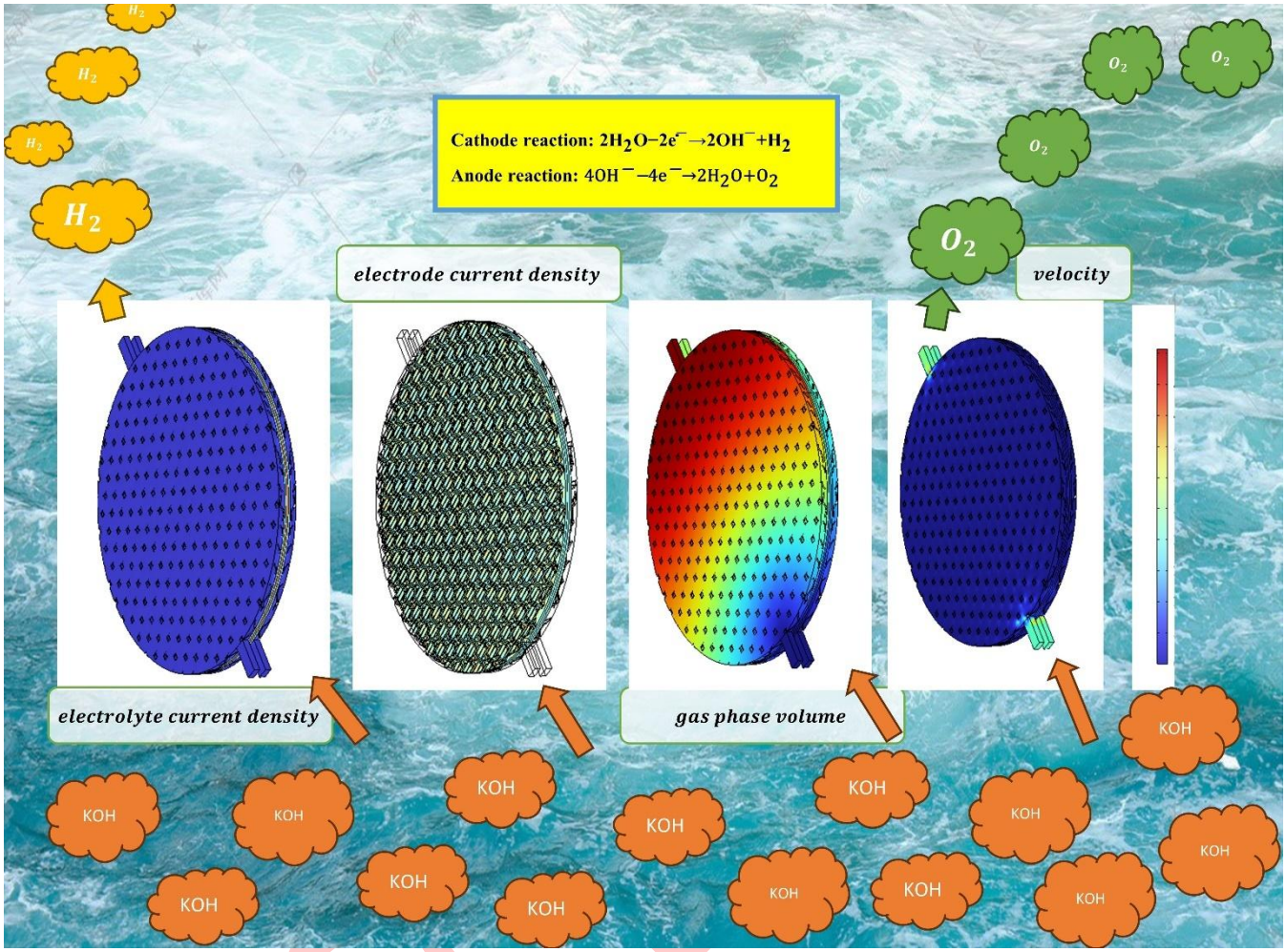

利用膨胀网作为双极板流道结构优化碱性水电解槽

熊海燕[a]，朱振啸[a]，高鑫[a]，范晨铭[a]，栾辉宝[b,*]，李冰[a,*]

（a. 华东理工大学，上海 200237；b. 上海，中国船舶有限公司第七一一研究所 201108）

摘要：碱性水电解制氢是现今最为成熟的水电解制氢技术。电解槽由多个电解小室组成，单个电解小室由隔膜、电极、双极板和端板等组成。现有工业的双极板流道结构为凹凸结构，通过模具冲压成型制备，制备成本高且困难。凹凸结构电解小室存在电解液流动不均匀和电流密度低的问题，进而增加了碱性水电解制氢的能耗和成本。因而，本文首先根据现有工业的凹凸双极板流道结构搭建电化学和流动模型，分析电解小室电流密度、电解液流动和气泡分布情况。模型可靠性已通过与文献实验数据对照验证。其中，电化学电流密度决定了气体产率，气体在电解液中流动反过来影响电化学反应活性比表面积和欧姆电阻。结果表明凹凸结构电解小室凹球底部流动速度几近为零，凸球表面电解液流速较大，流道结构中存在旋涡，电解液分布不均。接着，建模优化碱性水电解槽的流道结构，比较了凹凸结构、网状、菱形和膨胀网结构电解小室电化学和流动性能。结果表明，膨胀网结构电解小室电流密度最大，为 3330 A/m^2，电解液流速最大，为 0.507 m/s。相同电流密度下，过电位最小，能耗最低。本文对碱性水电解槽流道结构的全面理解和优化提供一定的指导意义，为大规模电解槽设计提供理论基础。

关键词：碱性水电解槽；膨胀网流道结构；数值模拟；